

Euler-Euler model of bubbly flow using particle-center-averaging method

Lyu, H.; Schlegel, F.; Rzehak, R.; Lucas, D.;

Originally published:

December 2022

Nuclear Science and Engineering 197(2023), 2602-2619

DOI: <https://doi.org/10.1080/00295639.2022.2131344>

Perma-Link to Publication Repository of HZDR:

<https://www.hzdr.de/publications/Publ-34742>

Release of the secondary publication
on the basis of the German Copyright Law § 38 Section 4.

Euler-Euler model of bubbly flow using particle-center-averaging method

Hongmei Lyu,^{*,a} Fabian Schlegel,^a Roland Rzehak,^a and Dirk Lucas^a

^a*Helmholtz-Zentrum Dresden - Rossendorf, Institute of Fluid Dynamics
Bautzner Landstrasse 400, D-01328 Dresden, Germany*

*Email: h.lyu@hzdr.de

Number of pages: 25

Number of tables: 3

Number of figures: 8

Abstract

The Euler-Euler model is widely used in bubbly flow simulations up to industrial dimensions. The standard Euler-Euler model is based on the phase-averaging method. After averaging, the bubble forces in the field equations are functions of the local gas volume fraction. In simulations, when the bubble diameter is larger than the computational cell spacing, the forces can transport the gas belonging to the same bubble in different directions. By contrast, a closure model for the bubble force is typically developed based on the assumption that the force is a resultant force that acts on the bubble's center-of-mass. This inconsistency can lead to a nonphysical gas concentration in the center of a channel or near the channel wall if the bubble diameter is larger than the cell spacing.

The purpose of the present contribution is to develop an Euler-Euler model where the bubble force consistency is recovered for two-phase flow simulations where the diameter of the disperse phase can be larger than the cell spacing. Such an Euler-Euler model is developed by combining an existing particle-center-averaged Euler-Euler framework with a Gaussian convolution method. To validate this Euler-Euler approach, a comparison is made with experimental data for the bubbly flows in two different vertical pipes. The results show that the proposed Euler-Euler model recovers the bubble force consistency and alleviates the over-prediction of the gas volume fraction peak near the wall, while its simulation results in the axial gas and liquid velocity and the liquid turbulence kinetic energy are similar to the results of the standard Euler-Euler model.

Keywords — bubbly flow simulation, Euler-Euler model, particle-center-averaging method, Gaussian convolution method, bubble's number density

I. INTRODUCTION

Gas-liquid bubbly flows are frequently encountered in the facilities of a nuclear power plant. For example, they appear in a boiling water reactor core and the steam generators of a pressurized water reactor. Exploring the flow mechanisms of the two-phase flows can ensure safety and improve the efficiency of these facilities. Benefiting from the affordable computational cost, the Euler-Euler model is widely used to study two-phase flows up to industrial dimensions. In the Euler-Euler model, the interface between the gas and the liquid is not resolved and the interfacial momentum interactions depend on the closure models for the bubble forces. Whereas, there is an inconsistency in the bubble force models used in the standard Euler-Euler simulation. A closure model for the bubble force is typically developed by tracking the trajectories of the bubbles' centers of mass and assuming that the force acts on these locations [1, 2, 3]. Whereas, the force becomes a function of the local gas volume fraction when it is applied in the standard Euler-Euler model. As a result, over-prediction of the gas volume fraction can appear in the center of a channel or near the channel wall when the bubble dimension is larger than the cell spacing in simulations [4, 5].

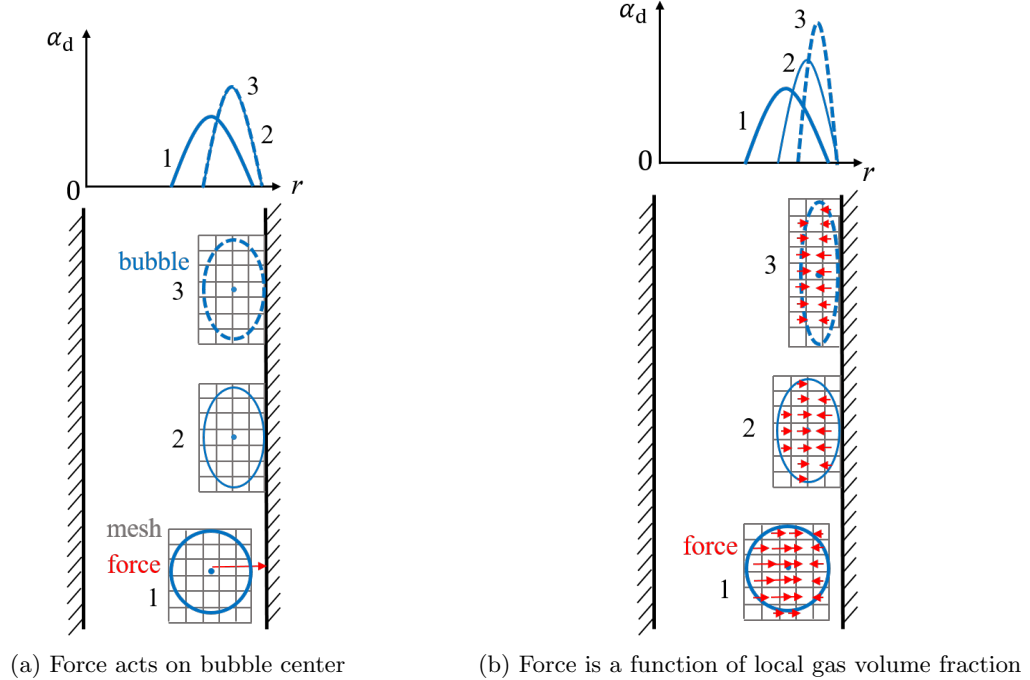


Fig. 1. Bubble Force Effects on Gas Volume Fraction Distribution

The phenomenon and the reason for the over-prediction of the gas volume fraction near the channel wall are shown in Fig. 1. In this condition, the bubble dimension is larger than the radial cell spacing. If the bubble force is the radial resultant force that acts on the bubble's center-of-mass (Fig. 1 a), after the bubble reaches the radial force balance location, the resultant force disappears and the bubble radial location will be the same in different downstream locations. In this condition, the radial profile for the bubble force should be unchanged in different downstream locations if the bubble has reached its terminal velocity. In contrast, if the bubble force is a function of the local gas volume fraction (Fig. 1 b), after the bubble reaches the force balance location for the radial resultant force, the bubble force still exists in the cells. This force will continue to transport the gas, which leads to the over-prediction of the gas volume fraction peak and a narrower peak near the wall. A similar phenomenon can appear in the center of a channel as well.

The forces act on the particle centers in the particle-center-averaged Euler-Euler framework developed by Prosperetti et al. [6, 7]. In this Euler-Euler approach, the phase-averaging method and the particle-center-averaging method are used to average the solution variables for the continuous phase and the disperse phase, respectively. However, a proper way to relate the quantities averaged by these different methods when the particle dimension is larger than the cell spacing is not provided. In the present study, the particle averaging method is represented by the specific term "particle-center-averaging method (PCAM)". Tomiyama et al. [4, 8] illustrated that the bubble force inconsistency can be removed if the bubble's number density is introduced in the continuity equation. In contrast, the disperse phase momentum equation they used is not related to the bubble's number density and it is equivalent to the equation of the standard Euler-Euler model. Therefore, the recovery they made is not comprehensive. In contrast, Lucas et al. [9, 10] introduced the bubble's number density into the momentum equation so that the bubble force acts on the bubble's centers-of-mass, but the solver they developed is only one-dimensional. A three-dimensional solver is required to study the bubbly flow more comprehensively.

To further develop an Euler-Euler model where the bubble force consistency is recovered for the bubbly flow simulations where the bubble diameter can be larger than the cell spacing, a way to relate a phase-averaged quantity and the corresponding particle-center-averaged quantity is needed. In previous studies, a bubble shape factor or a matrix that represents the fraction of the bubble volume inside a computational cell was used to calculate the gas volume fraction

from the bubble’s number density [4, 8, 10]. These ways to calculate the gas volume fraction are equivalent to a convolution using a kernel function that represents the spatial extent of a single bubble [11, 12]. However, these ways as well as the convolution method require high computational resources. Moreover, implementing the convolution method efficiently in a simulation code using unstructured grids is difficult if not impossible. In contrast, a diffusion-based method proposed by Sun et al. [13, 14] requires fewer computational resources and is easier to implement for both structured and unstructured grids. Moreover, it is theoretically equivalent to convolution with a Gaussian kernel function. Therefore, the diffusion-based method is used to realize the Gaussian convolution in this study.

In this study, the terms ”particle” and ”bubble” are used interchangeably since the averaged conservation equations are the same, but only applications for bubbly flows are considered. The present work further develops the particle-center-averaged Euler-Euler model for bubbly flow simulations by combining the particle-center-averaged Euler-Euler framework proposed by Prosperetti et al. [7] with a Gaussian convolution method. The entire approach is implemented based on the solver *multiphaseEulerFoam* in the OpenFOAM Foundation release [15]. The remaining part of this article is organized as follows. Section II introduces the theory of the particle-center-averaged Euler-Euler model. Section III presents the comparison between simulation results and experimental data. The conclusions of this work are given in Section IV.

II. THEORY OF THE PARTICLE-CENTER-AVERAGED EULER-EULER MODEL

II.A. Averaging Method

Compared to the standard Euler-Euler model, the different feature of the present particle-center-averaged Euler-Euler model is that the PCAM and the phase-averaging method are used to average the solution variables of the disperse phase and the continuous phase, respectively. For the average of the quantities related to the disperse phase (e.g. bubble’s center-of-mass velocity), each bubble is regarded as a whole and the quantities are attached to the bubble’s center. Therefore, a Dirac delta function δ indicating the location of the bubble center is involved in the averaging.

The ensemble particle-center-average of a quantity Φ for the disperse phase is defined by [7]

$$\langle \Phi_d \rangle (\mathbf{x}, t) = \frac{1}{n(\mathbf{x}, t)} \int_{C^N} \left[\sum_{b=1}^N \delta(\mathbf{x} - \mathbf{y}^b) \Phi^b(N; t) \right] P(N; t) dC^N. \quad (1)$$

Herein, the notation " $\langle \cdot \rangle$ " indicates the particle-center-averaged quantity and a subscript d denotes the disperse phase. In Eq. (1), \mathbf{x} is the spatial coordinate vector, t is the physical time, n is the number density of the bubble centers, C^N describes the set of all possible dynamic states for a system containing N indistinguishable bubbles, \mathbf{y}^b is the coordinate vector of the center location for bubble b , Φ^b is the value of the quantity Φ for bubble b ($b = \{1, \dots, N\}$), and $P(N; t)$ is the probability density function of a dynamic state at time t . The involved Dirac delta function has the following property:

$$\delta(\mathbf{x} - \mathbf{y}^b) = \begin{cases} \infty, & \mathbf{x} = \mathbf{y}^b; \\ 0, & \text{otherwise.} \end{cases} \quad (2)$$

The bubble's number density is defined by

$$n(\mathbf{x}, t) = \int P(\mathbf{x}, \mathbf{u}^b, t) d\mathbf{u}^b. \quad (3)$$

Here \mathbf{u}^b is the center-of-mass velocity for bubble b , while $P(\mathbf{x}, \mathbf{u}^b, t)$ is one-bubble probability density function, which is related to $P(N; t)$ as

$$P(\mathbf{x}, \mathbf{u}^b, t) = \int P(N; t) dC^{N-1}. \quad (4)$$

In addition, the relation

$$\int_{\Omega} n d\Omega = N \quad (5)$$

justifies that n is the bubble's number density. Herein, Ω is the fluid domain.

According to Prosperetti et al. [7], the ensemble phase-average of a quantity Φ for the continuous phase is defined by

$$\overline{\Phi_c}(\mathbf{x}, t) = \frac{1}{\alpha_c(\mathbf{x}, t)} \int_{C^N} \Phi_c(\mathbf{x}, t; N) X_c(\mathbf{x}; N) P(N; t) dC^N, \quad (6)$$

where the overbar " $\overline{\cdot}$ " indicates the phase-averaged quantity and a subscript c denotes the con-

tinuous phase. In Eq. (6), X_c is the phase indicator function. Its value is 1 where the continuous phase exists; otherwise, it is 0.

II.B. Field Equations

The field equations for Newtonian fluids from Prosperetti et al. [7] are summarized in this subsection. The continuity equations for both phases are

$$\frac{\partial n \rho_d}{\partial t} + \nabla \cdot n \rho_d \langle \mathbf{u}_d \rangle = 0, \quad (7)$$

and

$$\frac{\partial \alpha_c \rho_c}{\partial t} + \nabla \cdot \alpha_c \rho_c \overline{\mathbf{u}_c} = 0, \quad (8)$$

where ρ is the density and \mathbf{u} is the velocity. The momentum equation for the disperse phase is

$$\frac{\partial \beta_d \rho_d \langle \mathbf{u}_d \rangle}{\partial t} + \nabla \cdot \beta_d \rho_d \langle \mathbf{u}_d \rangle \langle \mathbf{u}_d \rangle = -\beta_d \nabla \overline{p_c} + \beta_d \nabla \cdot \overline{\mathbf{S}_c} + \nabla \cdot \beta_d \langle \mathbf{T}_d \rangle + \langle \mathbf{f}_d \rangle + \beta_d \rho_d \mathbf{g}, \quad (9)$$

where

$$\beta_d = n V_B. \quad (10)$$

Herein, p , \mathbf{S} , \mathbf{T} , \mathbf{f} , \mathbf{g} and V_B are the pressure, the viscous stress tensor, the Reynolds stress tensor, the force per unit control volume, the acceleration of gravity and the bubble volume, respectively. The momentum equation for the continuous phase reads

$$\frac{\partial \alpha_c \rho_c \overline{\mathbf{u}_c}}{\partial t} + \nabla \cdot \alpha_c \rho_c \overline{\mathbf{u}_c} \overline{\mathbf{u}_c} = -\alpha_c \nabla \overline{p_c} + \alpha_c \nabla \cdot \overline{\mathbf{S}_c} + \nabla \cdot \alpha_c \overline{\mathbf{T}_c} + \overline{\mathbf{f}_c} + \alpha_c \rho_c \mathbf{g}. \quad (11)$$

In this study, both phases are regarded as incompressible and a fixed monodisperse bubble size is assumed. Heat transfer, bubble swarm effects, as well as bubble coalescence and breakup are not involved.

II.C. Closure Models

The number of the field equations (Eqs. (7), (8), (9) and (11)) is 4, while the number of the unknown variables (n , \mathbf{u}_d , $\langle \mathbf{T}_d \rangle$, $\langle \mathbf{f}_d \rangle$, α_c , $\overline{\mathbf{u}_c}$, $\overline{p_c}$, $\overline{\mathbf{S}_c}$, $\overline{\mathbf{T}_c}$ and $\overline{\mathbf{f}_c}$) is 10. To obtain a solution for

the two-phase flow problem, 6 closure equations are required to close the problem. As summarized in Prosperetti et al. [7], $\langle \mathbf{T}_d \rangle$ is usually assumed to be zero for particle flow, which is similar to the derivation result of the spherical drops in Stokes flow and the spherical bubbles in potential flow. This assumption coincides with Helmholtz-Zentrum Dresden-Rossendorf (HZDR) baseline model [16] where a laminar model is used to simulate the flow of the disperse phase. Therefore, the assumption

$$\langle \mathbf{T}_d \rangle = 0 \quad (12)$$

is employed in this study.

The interfacial momentum interactions are assumed to be represented by a linear combination of the different contributions as follows:

$$\langle \mathbf{f}_d \rangle = \langle \mathbf{f}_d^D \rangle + \langle \mathbf{f}_d^{SL} \rangle + \langle \mathbf{f}_d^{WL} \rangle + \langle \mathbf{f}_d^{VM} \rangle + \langle \mathbf{f}_d^{TD} \rangle + \langle \mathbf{f}_d^{WC} \rangle. \quad (13)$$

Herein, \mathbf{f}^D , \mathbf{f}^{SL} , \mathbf{f}^{WL} , \mathbf{f}^{VM} , \mathbf{f}^{TD} and \mathbf{f}_d^{WC} are the drag, the shear-lift, the wall-lift, the virtual mass, the turbulent dispersion force and the wall-contact force per unit control volume, respectively. The closure models for these forces are selected according to HZDR baseline model [16] listed in Table I. As mentioned in Section I, the bubble force model developed in the literature is usually a resultant force for a single bubble, which is the case for the selected drag, shear-lift, wall-lift and virtual mass force model here. To convert the developed force model to the force in the disperse phase momentum equation, the following relation is used:

$$\langle \mathbf{f}_d \rangle = n \mathbf{F}_B. \quad (14)$$

Herein, \mathbf{F}_B is the resultant force for a single bubble. The turbulent dispersion force model proposed by Burns et al. [17] is suitable for the standard Euler-Euler simulation because the first averaging method for the drag force is phase-averaging. Based on their derivation procedure, a turbulent dispersion force model for the Euler-Euler model based on PCAM is derived. The resulting model is

$$\langle \mathbf{f}_d^{TD} \rangle = -\frac{3\beta_d}{4d_B} C_D \rho_c |\langle \mathbf{u}_d \rangle - \langle \mathbf{u}_c \rangle| \frac{\langle \nu_c^{\text{turb}} \rangle}{\sigma_{\alpha c}} \left(\frac{\nabla \beta_d}{\beta_d} - \frac{\nabla \alpha_c}{\alpha_c} \right). \quad (15)$$

Herein, d_B is the bubble diameter, C_D is the drag coefficient, ν_c^{turb} is the turbulent eddy viscosity

TABLE I
HZDR Baseline Model for Bubbly Flow Simulations

Force and turbulence	Selected model
Drag force	Ishii and Zuber [19]
Shear-lift force	Hessenkemper et al. [20] with cosine wall damping
Turbulent dispersion force	
Wall-lift force	Burns et al. [17]
Virtual mass force	Hosokawa et al. [2]
Shear-induced turbulence	Constant coefficient, $C_{VM} = 0.5$ [21]
Bubble-induced turbulence	$k - \omega$ SST [22]
	Ma et al. [23]

and σ_{ac} is the Schmidt number. The Schmidt number is typically set to be 0.9 and used in the following simulations [18].

The wall-contact force model proposed by Lucas et al. [10] is adapted for bubbles with an oblate ellipsoidal shape and used in the Euler-Euler simulations based on PCAM. The resulting wall-contact force reads

$$\langle \mathbf{f}_d^{WC} \rangle = n\pi d_B \sigma \left\{ \frac{1}{\tilde{L}^2} - \frac{3\tilde{L}}{2G} \left[\left(\frac{4\sqrt{G}}{3} + \frac{\tilde{L}^3}{\sqrt{G}} \right) \operatorname{arctanh}(\sqrt{G}) - 1 \right] \right\} \mathbf{n}_w, \quad (16)$$

where $\tilde{L} = 2L/d_B$, $G = 1 - \tilde{L}^3$, L is the distance between the bubble's center-of-mass and the wall, σ is the surface tension coefficient, and \mathbf{n}_w is the unit wall-normal vector pointing into the fluid.

By assuming that the phase-averaged strain rate is approximated by the strain rate of the phase-averaged velocity, we obtain the following relation for the viscous stress tensor of the continuous phase:

$$\overline{\mathbf{S}}_c = \mu_c \left[\nabla \overline{\mathbf{u}}_c + (\nabla \overline{\mathbf{u}}_c)^T - \frac{2}{3} \mathbf{I} \nabla \cdot \overline{\mathbf{u}}_c \right]. \quad (17)$$

Herein, μ is the dynamic viscosity and \mathbf{I} is a unit tensor. The Reynolds stress for the continuous phase is approximated by the Boussinesq assumption:

$$\overline{\mathbf{T}}_c = -\frac{2}{3} \rho_c \overline{k}_c \mathbf{I} + \overline{\mu}_c^{\text{turb}} \left[\nabla \overline{\mathbf{u}}_c + (\nabla \overline{\mathbf{u}}_c)^T - \frac{2}{3} \mathbf{I} \nabla \cdot \overline{\mathbf{u}}_c \right]. \quad (18)$$

Herein, k is the turbulence kinetic energy, and μ^{turb} is the turbulent viscosity. As shown in Table I, $k - \omega$ SST turbulence model is employed together with the bubble-induced turbulence model of Ma et al. [23] to further calculate \overline{k}_c and $\overline{\mu}_c^{\text{turb}}$.

So far, we have 4 closure relations (Eqs. (12), (13), (17) and (18)). The remaining 2 closure

relations are established by relating n and α_c as well as relating $\langle \mathbf{f}_d \rangle$ and $\overline{\mathbf{f}_c}$, which will be introduced in Subsection II.D.

II.D. Conversion between Phase-averaged and Particle-center-averaged Quantities

Convolution with a Gaussian kernel is used to convert a particle-center-averaged quantity to the corresponding phase-averaged quantity. In three-dimensional space, by solving a diffusion equation, the relation between a phase-averaged quantity ($\overline{\Phi}$) and the corresponding particle-center-averaged quantity ($\langle \Phi \rangle$) is established by

$$\overline{\Phi}(\mathbf{x}, \tau) = \int_{\Omega} \langle \Phi \rangle(\mathbf{x}_0) \frac{1}{(4\pi C_{\text{diff}} \tau)^{\frac{3}{2}}} \exp \left[-\frac{(\mathbf{x} - \mathbf{x}_0)^2}{4C_{\text{diff}} \tau} \right] d\mathbf{x}_0, \quad (19)$$

where \mathbf{x}_0 are the spatial locations, while C_{diff} and τ are the diffusion coefficient and the diffusion pseudo-time, respectively. In this way, the gas volume fraction is related to the bubble's number density by

$$\alpha_d(\mathbf{x}, \tau) = \int_{\Omega} n(\mathbf{x}_0) V_B \frac{1}{(4\pi C_{\text{diff}} \tau)^{\frac{3}{2}}} \exp \left[-\frac{(\mathbf{x} - \mathbf{x}_0)^2}{4C_{\text{diff}} \tau} \right] d\mathbf{x}_0. \quad (20)$$

With Eq. (20) and the relation $\alpha_c = 1 - \alpha_d$, the relation between α_c and n is determined.

Similarly, the phase-averaged force of the disperse phase is related to the particle-center-averaged force by

$$\overline{\mathbf{f}_d}(\mathbf{x}, \tau) = \int_{\Omega} \langle \mathbf{f}_d \rangle(\mathbf{x}_0) \frac{1}{(4\pi C_{\text{diff}} \tau)^{\frac{3}{2}}} \exp \left[-\frac{(\mathbf{x} - \mathbf{x}_0)^2}{4C_{\text{diff}} \tau} \right] d\mathbf{x}_0. \quad (21)$$

With Eq. (21) and the relation $\overline{\mathbf{f}_c} = -\overline{\mathbf{f}_d}$, the relation between $\overline{\mathbf{f}_c}$ and $\langle \mathbf{f}_d \rangle$ is determined. Besides, the phase-averaged gas velocity is related to the particle-center-averaged gas velocity by

$$\overline{\mathbf{u}_d}(\mathbf{x}, \tau) = \frac{1}{\alpha_d(\mathbf{x}, \tau)} \int_{\Omega} n(\mathbf{x}_0) V_B \langle \mathbf{u}_d \rangle(\mathbf{x}_0) \frac{1}{(4\pi C_{\text{diff}} \tau)^{\frac{3}{2}}} \exp \left[-\frac{(\mathbf{x} - \mathbf{x}_0)^2}{4C_{\text{diff}} \tau} \right] d\mathbf{x}_0. \quad (22)$$

On the contrary, the weighted-average velocity of the continuous phase at the bubbles' centers of mass $\langle \mathbf{u}_c \rangle$ is required when calculating the force in the bubbles' centers $\langle \mathbf{f}_d \rangle$. The velocity can be calculated from the corresponding phase-averaged continuous phase velocity $\overline{\mathbf{u}_c}$ by the following

Gaussian convolution:

$$\langle \mathbf{u}_c \rangle (\mathbf{x}_0, \tau) = \int_{\Omega} \overline{\mathbf{u}_c}(\mathbf{x}) \frac{1}{(4\pi C_{\text{diff}} \tau)^{\frac{3}{2}}} \exp \left[-\frac{(\mathbf{x} - \mathbf{x}_0)^2}{4C_{\text{diff}} \tau} \right] d\mathbf{x}_0, \quad (23)$$

As is shown in above equations, the quantity converted by the Gaussian convolution which is realized by the diffusion-based method depends on C_{diff} and τ . Without loss of generality, C_{diff} is set to be $1 \text{ m}^2 \text{ s}^{-1}$ for all diffusion processes in the present study, while the optimized value for τ , which is $0.03356 \times d_B^2 / C_{\text{diff}}$, is used. Note, the optimized diffusion time is related to C_{diff} . Therefore, if the C_{diff} is set to be another value instead of $1 \text{ m}^2 \text{ s}^{-1}$, the optimized diffusion time will be adjusted correspondingly. At last, the conversion results will be the same under the different chosen value for C_{diff} and the corresponding optimized diffusion time.

III. SIMULATION RESULTS COMPARED TO MEASUREMENTS

This section considers bubbly flows in different vertical pipes to evaluate the Euler-Euler model based on PCAM. For the bubbly flow cases, the experimental conditions and simulation setups are presented. Afterward, the predictions of the standard Euler-Euler model and the Euler-Euler model based on PCAM are compared with experimental data and discussed.

III.A. Description of the Experiments

Experimental data are from the measurement test loop (MTLoop) facility [24, 25] as well as from the experiments reported by Hosokawa et al. [26]. For both test facilities, the test section is a vertical pipe. The inner diameter of the pipe in the MTLoup experiment is about 2 times that of the experiment of Hosokawa et al. The experimental conditions are summarized in Table II. A schematic for the test facility is shown in Fig. 2. In the experiments, water from a water tank at around room temperature and atmospheric pressure is supplied to the test section by a circulation pump. Air is compressed by a compressor and injected into the test section from the bottom. After the air-water mixture leaves the test section, the water comes back to the tank where a heat exchanger is used to control the temperature. Meanwhile, the air is released into the environment.

The experimental data were obtained by different techniques, including intrusive and non-invasive methods. In the MTLoup experiment, the bubble characteristics, including local gas

TABLE II
Experimental Conditions (LDV: laser Doppler velocimetry system)

Experimental conditions	MTLoop experiment	Experiment of Hosokawa et al.
Disperse phase	air	air
Continuous phase	water	tap water
Temperature [K]	303.15	298.15
Pressure [Pa]	101325	101325
Pipe inner diameter [mm]	51.2	25.0
Pipe length [m]	3.5	2.0
Measurement plane [m]	3.03	1.7
Bubble characteristic measurement	wire-mesh sensors	image processing method
Liquid characteristic measurement	-	LDV

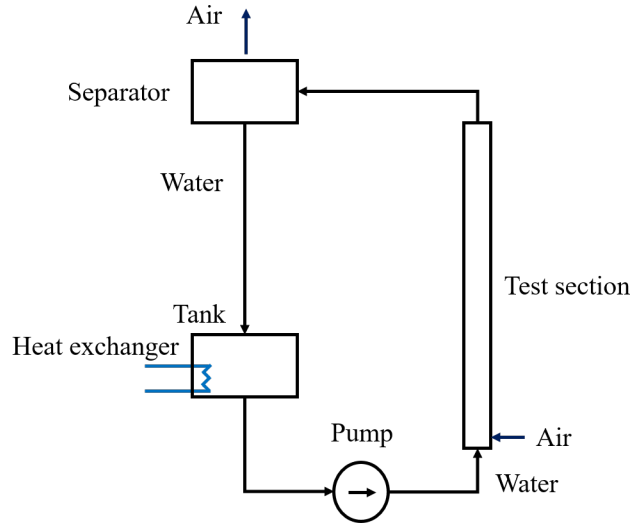


Fig. 2. Schematic of Test Facility.

volume fraction, bubble size, and axial bubble velocity, were obtained at several axial heights by the wire-mesh sensor with two measurement planes. In the experiment of Hosokawa et al., the pipe of the test section was made of FEP (fluorinated ethylene-propylene resin). It is transparent and its refractive index is close to that of water. The bubble images were recorded by two high-speed cameras. The bubble characteristics were obtained by post-processing the recorded images. The liquid velocities were obtained by a laser Doppler velocimetry system (LDV).

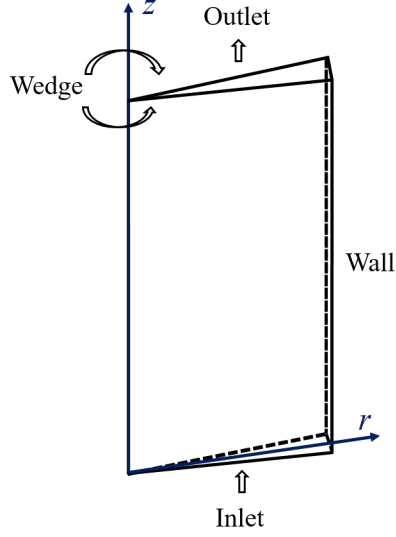


Fig. 3. Geometry and Boundary Settings

III.B. Simulation Setup

III.B.1. Models and Numerical Scheme

As mentioned in Subsection II.C, the HZDR baseline model together with a wall-contact force is employed in the particle-center-averaged Euler-Euler simulations. For the standard Euler-Euler simulation, the HZDR baseline model is also employed. The bubble shape model proposed by Ziegenhein et al. [27] and the pressure treatment of Rzehak et al. [28] are used.

For the discretization of the convection terms, a flux-limiter is used to make the simulations stable. A first-order Euler implicit scheme is used for temporal discretization. Similarly, for the discretization of the diffusion equations solved for the quantity conversions, a first-order Euler implicit scheme is used for the temporal discretization and a Gauss linear scheme is used for the discretization of the Laplacian term.

III.B.2. Geometry and Boundary Condition

The flows in the locations where a comparison is made for simulation results and experimental data are regarded as fully developed and circumferentially symmetric. Therefore, to save computational cost, the computational domain for the simulations is a narrow sector of the test-section pipe with wedge boundary conditions imposed on the side faces. The same was done in previous

studies [5, 29, 18]. The geometry and boundary settings are shown in Fig. 3. The simulations for the MTLoop experiment feature a center angle of the wedge of 1.0° , while the simulations based on the experiment of Hosokawa et al. have a center angle of 2.5° . The different choices for the central angle are not on purpose and they should not make any difference in the simulation results. According to the test results (not shown here), the simulation results of some MTLoop cases with the central angle equal to 1.0° are about the same as that with the central angle equal to 2.5° .

The inlet velocities and volume fractions are calculated from the superficial velocities obtained in the experiments. At the inlet, the spatial distributions of the velocities and the volume fractions are uniform. In addition, by assuming a vanishing relative velocity between air and water, the axial velocities are calculated by

$$u_d = u_c = J_d + J_c, \quad (24)$$

where J is the superficial velocity. The inlet gas volume fraction is computed by

$$\alpha_d = \frac{J_d}{J_d + J_c}. \quad (25)$$

III.B.3. Computational Mesh and Selected Cases

A quasi-two-dimensional mesh is applied to the computational domain for the simulations. Only one layer of computational cells is used in the circumferential direction. Besides, the cell spacing is uniform in the axial and radial directions. For the simulations of MTLoop experimental cases, the numbers of grid cells in the radial and axial directions are 50 and 800, respectively. For the simulation of the experimental cases of Hosokawa et al., the numbers of grid cells in both directions are 40 and 800, respectively. The simulation results with these mesh resolutions are mesh-independent.

The detailed parameters for the selected cases are listed in Table III. The name of the MTLoop cases starts with "MT", while the name of the experimental cases of Hosokawa et al. begins with "HO". As is shown in Table III, the ratio between the bubble diameter and the radial cell spacing is larger than 7. Therefore, the chosen mesh resolutions are suitable for the simulations to reveal the nonphysical phenomena caused by the inconsistency of the bubble force models used in the standard Euler-Euler simulations. They are also proper for the simulations to illustrate the ability of the PCAM in recovering the consistency.

TABLE III
Parameters for the Selected Cases (Δ_r : radial cell spacing)

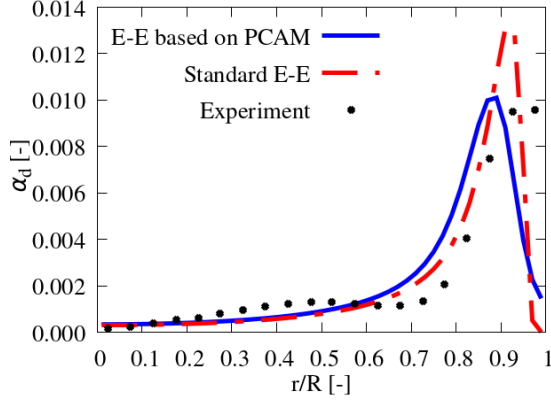
Name	J_c [m s ⁻¹]	J_d [m s ⁻¹]	d_B [mm]	d_B/Δ_r [-]
MT19	1.017	0.004	4.44	8.7
MT42	1.611	0.0096	3.89	7.6
MT64	1.611	0.0235	4.40	8.6
MT98	2.554	0.0898	4.01	7.8
MT109	2.554	0.14	4.38	8.6
MT120	2.554	0.219	4.78	9.3
HO11	0.5	0.018	3.21	10.3
HO12	0.5	0.025	4.25	13.6
HO21	1.0	0.02	3.52	11.3
HO22	1.0	0.036	3.66	11.7

III.C. Comparison of Simulation Results and Experimental Data

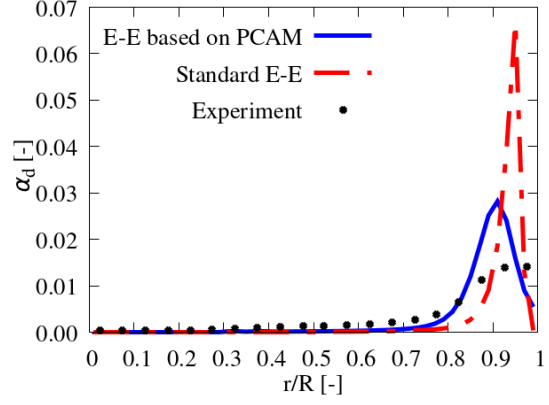
III.C.1. Gas Volume Fraction

Figure 4 shows the profiles for the gas volume fractions simulated with the Euler-Euler model based on PCAM and the standard Euler-Euler model in comparison with the profiles obtained in the MTLoop experiment. Herein, r is the radial coordinate and R is the pipe radius. For all cases, the deviation between the simulation results and the experimental data appears in the region near the gas volume fraction peaks. The peak of the gas volume fraction profiles simulated with the standard Euler-Euler model is higher than the peak in the experimental data. The simulated peak is about 1.37, 4.72, 2.30, 6.38, 3.95 and 2.13 times the peak in the experimental data for cases MT19, MT42, MT64, MT98, MT109 and MT120, respectively. Herein, the maximum of the simulation results and the measurement data are used in the comparisons and these maxima can appear in different radial locations. In addition, for case MT42, the simulated peak is narrower than the peak in the experimental data. The reason for the over-predicted and narrow peaks is that the shear-lift force and the wall-lift force drive the gas to the peak without considering the bubble dimension because these forces are functions of the local gas volume fraction.

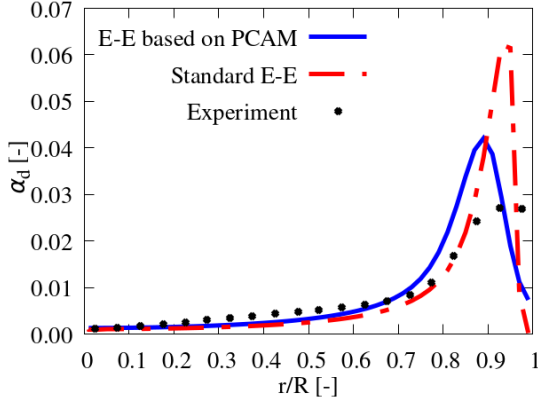
After using the PCAM in the Euler-Euler simulations, the over-prediction of the gas volume fraction peaks is alleviated. The simulated peak turns to be around 1.05, 1.99, 1.55, 3.87, 2.73 and 1.65 times the peak in the experimental data for the cases. Moreover, for case MT42, the width of the simulated peak agrees well with the experimental data. The reason is that using the PCAM in the Euler-Euler simulations changes the bubble forces to act on the bubbles' centers of mass by



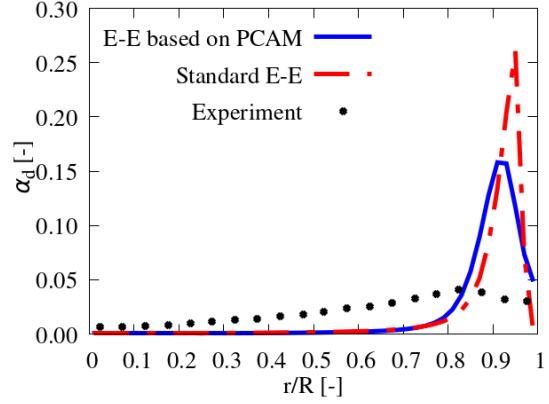
(a) MT19



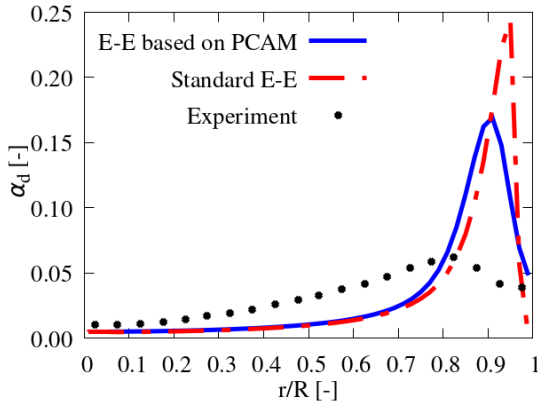
(b) MT42



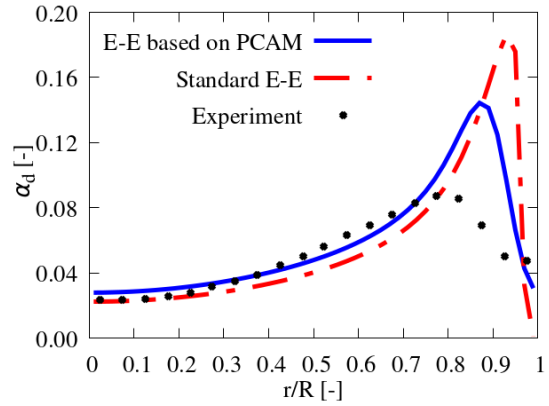
(c) MT64



(d) MT98



(e) MT109



(f) MT120

Fig. 4. Gas Volume Fraction for MTLoop Experimental Cases ("E-E": Euler-Euler model).

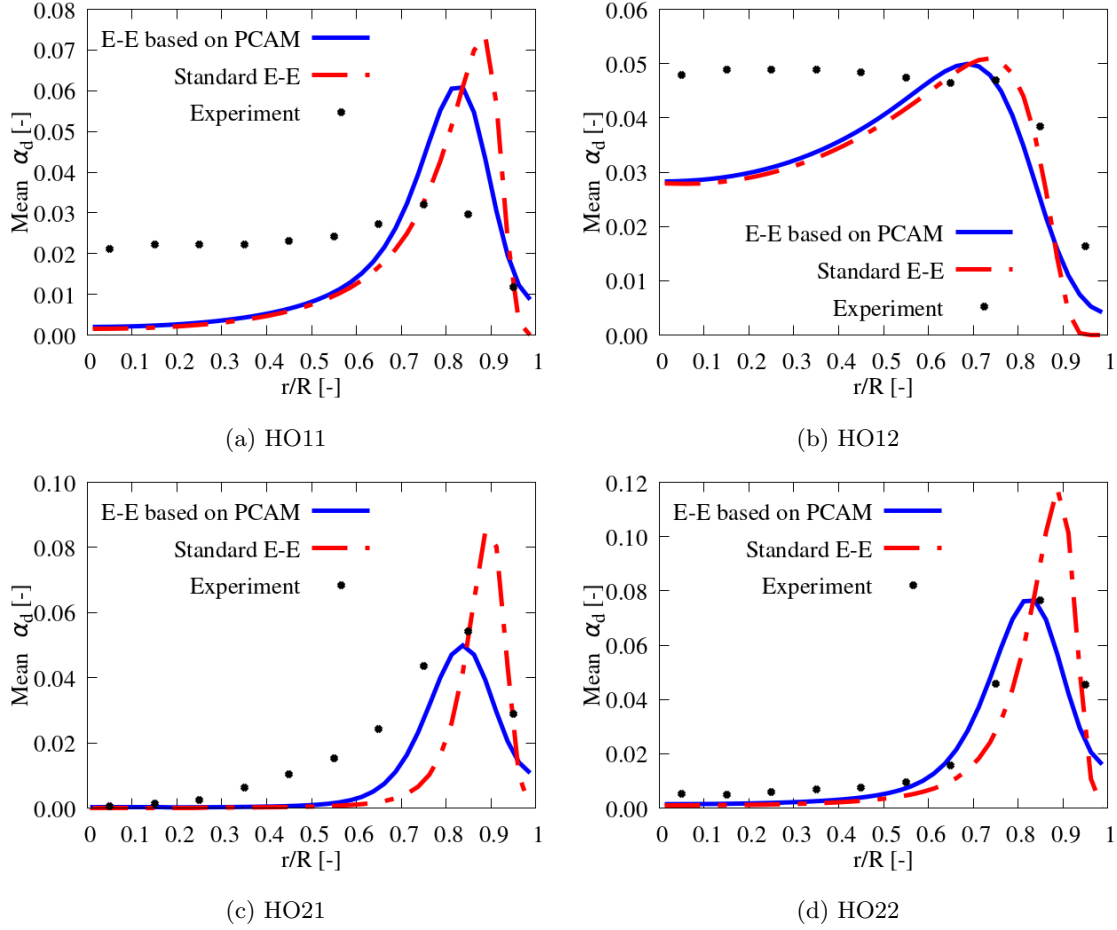


Fig. 5. Mean Gas Volume Fraction for Experimental Cases of Hosokawa et al. (“E-E”: Euler-Euler model).

introducing the bubble’s number density.

The gas volume fractions simulated by both Euler-Euler models together with the data obtained in the experiment of Hosokawa et al. are shown in Fig. 5. The simulation results were averaged between 6 s and 10 s of simulation time because the standard Euler-Euler simulations for cases HO21 and HO22 did not reach a steady state. For case HO12, the simulated gas volume fraction profiles with both Euler-Euler models are close to each other, and the simulation results are close to the experimental data near the wall with $0.5 < r/R < 1$, but they are under-predicted in the pipe-center region. The reason for the deviation is that the drag force used in the simulations is not strong enough. The simulated gas velocity is over-estimated, which leads to the under-prediction of gas volume fraction when the gas volumetric flow rate is fixed.

For the remaining cases, the gas volume fraction peak simulated with the standard Euler-Euler model is higher and narrower than the peak in the experimental data. It is about 2.29, 1.56, and 1.54 times the peak in the experimental data for cases HO11, HO21, and HO22, respectively. Similar to the condition in the MTLoop cases, the reason for the over-predictions is that the bubble forces are functions of the local gas volume fraction, and the shear-lift and the wall-lift force induce gas over-concentration near the wall peak. After changing the bubble forces to act on the bubbles' centers of mass by the PCAM, the over-prediction of the gas volume fraction peak for case HO11 is alleviated. The simulated peak is 1.89 times the peak in the experimental data. However, for case HO11, the gas volume fractions simulated with both Euler-Euler models are over-estimated near the wall and under-estimated in the pipe center region with $0 < r/R < 0.6$. This results from the fact that in the simulations, the shear-lift force is too strong or the wall-lift force is not strong enough. For cases HO21 and HO22, the gas volume fraction peaks simulated with the PCAM are close to the peaks in the experimental data. Furthermore, compared with the standard Euler-Euler simulation results, the shape of the gas volume fraction profile for cases HO21 and HO22 simulated with the PCAM is closer to the shape of the measurement profiles.

III.C.2. Axial Gas Velocity

Figure 6 shows the axial gas velocity profiles simulated by both Euler-Euler models in comparison with the data obtained in the experiment. For cases MT19 and MT42, near the wall with $0.90 < r/R < 0.95$, the gas velocities simulated with the standard Euler-Euler model are slightly higher than the results of the Euler-Euler model based on PCAM. The reason is that in this region, the gas volume fraction simulated with the standard Euler-Euler model is higher, which induces a higher buoyancy force for the gas phase. Overall, the axial gas velocities simulated with both Euler-Euler models are almost the same and agree well with the experimental data.

For cases HO21 and HO22, in the pipe-center region with $0 < r/R < 0.8$, the gas velocities simulated with both Euler-Euler models are approximately the same. Near the wall, a difference appears in the simulated gas velocities. Similar to the results of cases MT19 and MT42, in the region with $0.80 < r/R < 0.92$, the gas velocities simulated with the standard Euler-Euler model are higher than that simulated with the Euler-Euler model based on PCAM. This also corresponds to the high gas volume fractions simulated with the standard Euler-Euler model.

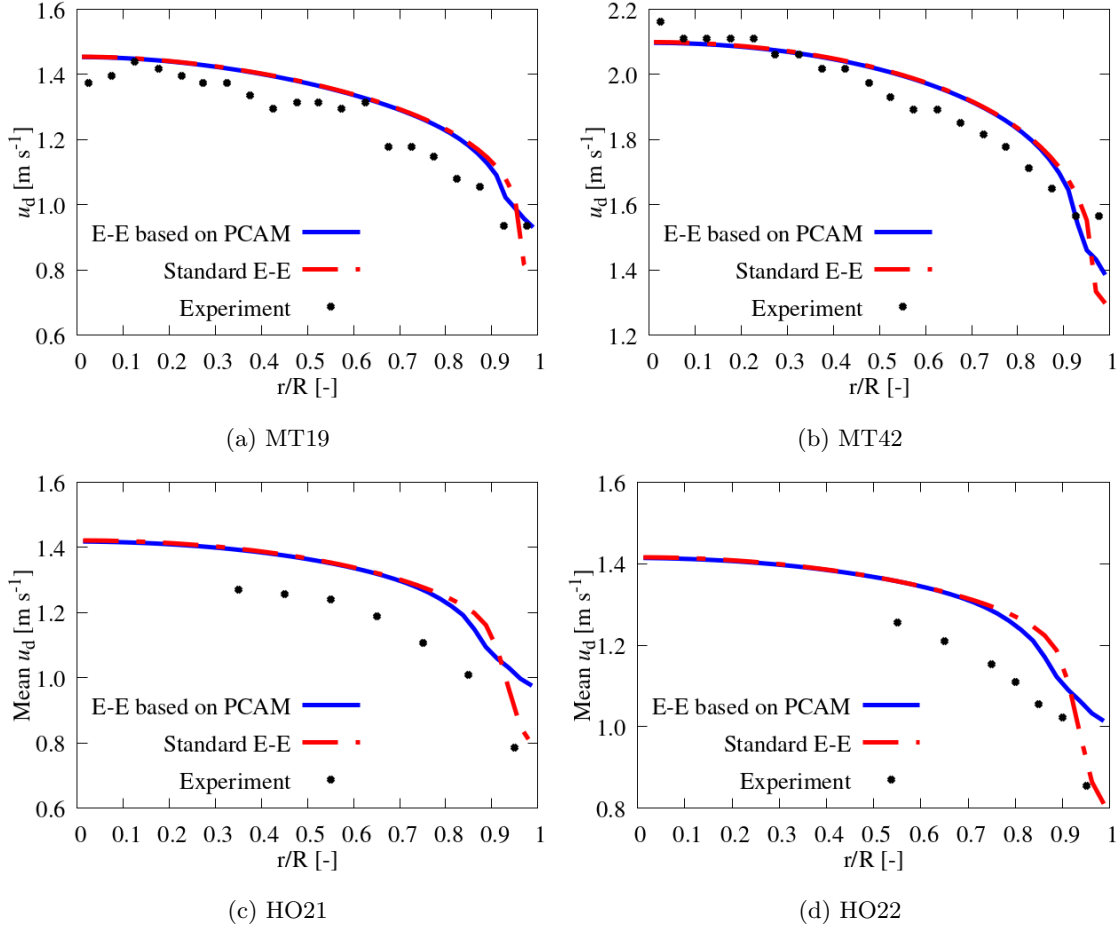


Fig. 6. Axial Gas Velocity for Experimental Cases of MTLoop ("E-E": Euler-Euler model).

In this region, the gas velocities simulated with the Euler-Euler model based on PCAM fit the experimental data better than the results of the standard Euler-Euler model. For both cases, the results simulated with both Euler-Euler models are over-predicted. The deviation is higher than the reported measurement uncertainty which is 3% [26], but further analysis is stopped by the fact that the measurement data do not cover the whole cross-section of the pipe.

III.C.3. Axial Liquid Velocity

For axial liquid velocity, the comparison between the simulation results and data obtained in the experiment of Hosokawa et al. is shown in Fig. 7. The liquid velocities simulated with both Euler-Euler models match. In addition, the simulation results are slightly over-predicted, but the shape of the simulated and measurement profiles are similar. The deviation between the

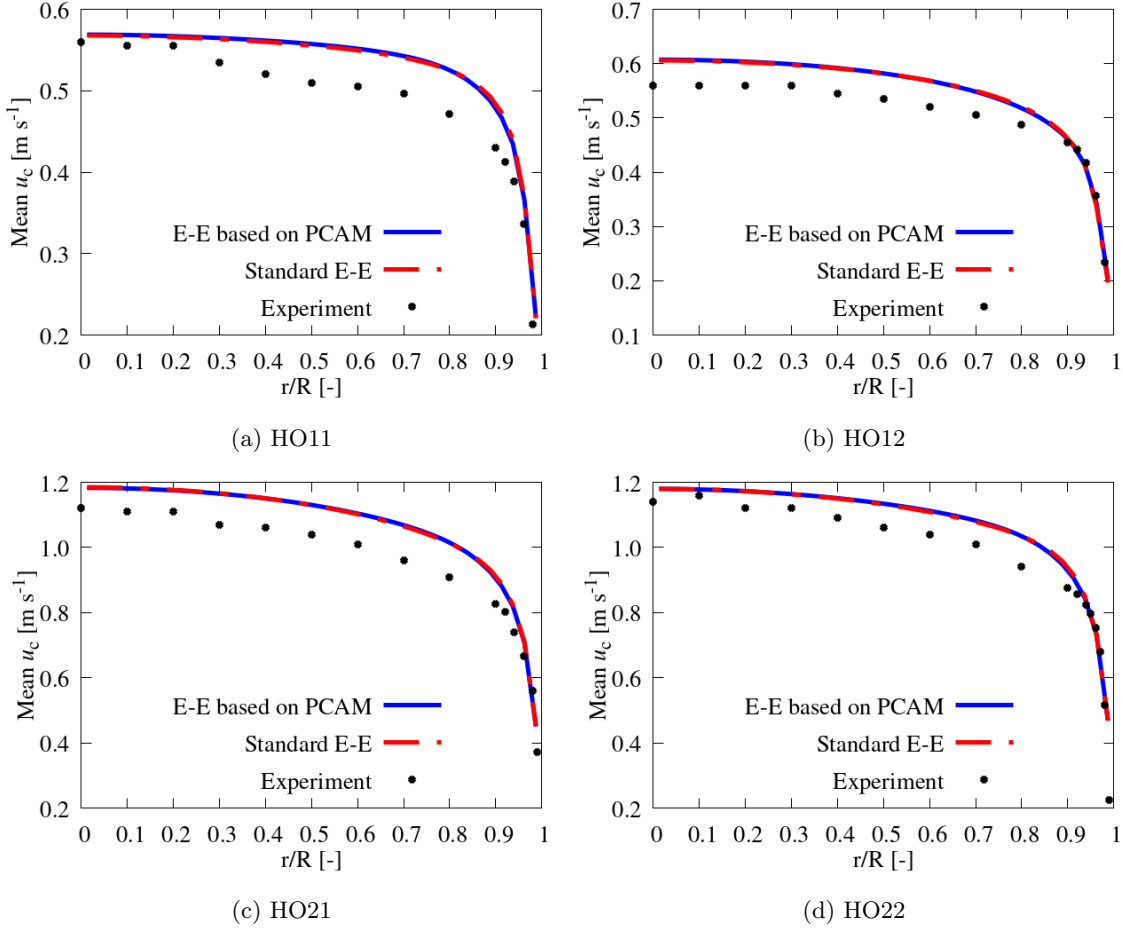


Fig. 7. Axial Liquid Velocity for Experimental Cases of Hosokawa et al. ("E-E": Euler-Euler model).

simulation results and the experimental data may come from the measurement uncertainty in the data. Although the reported uncertainty of the measurement liquid velocity is around 1% [26], for case HO11, the liquid volumetric flow rate calculated from the measurement axial liquid velocity and liquid volume fraction is about 5% lower than the flow rate calculated from the superficial liquid velocity. Based on this situation, it is speculated that the measurement liquid velocities are slightly lower than the expected values.

III.C.4. Liquid Turbulence Kinetic Energy

Figure 8 gives the profiles for the liquid turbulence kinetic energy simulated by both Euler-Euler models in comparison with the data obtained in the experiment of Hosokawa et al. The

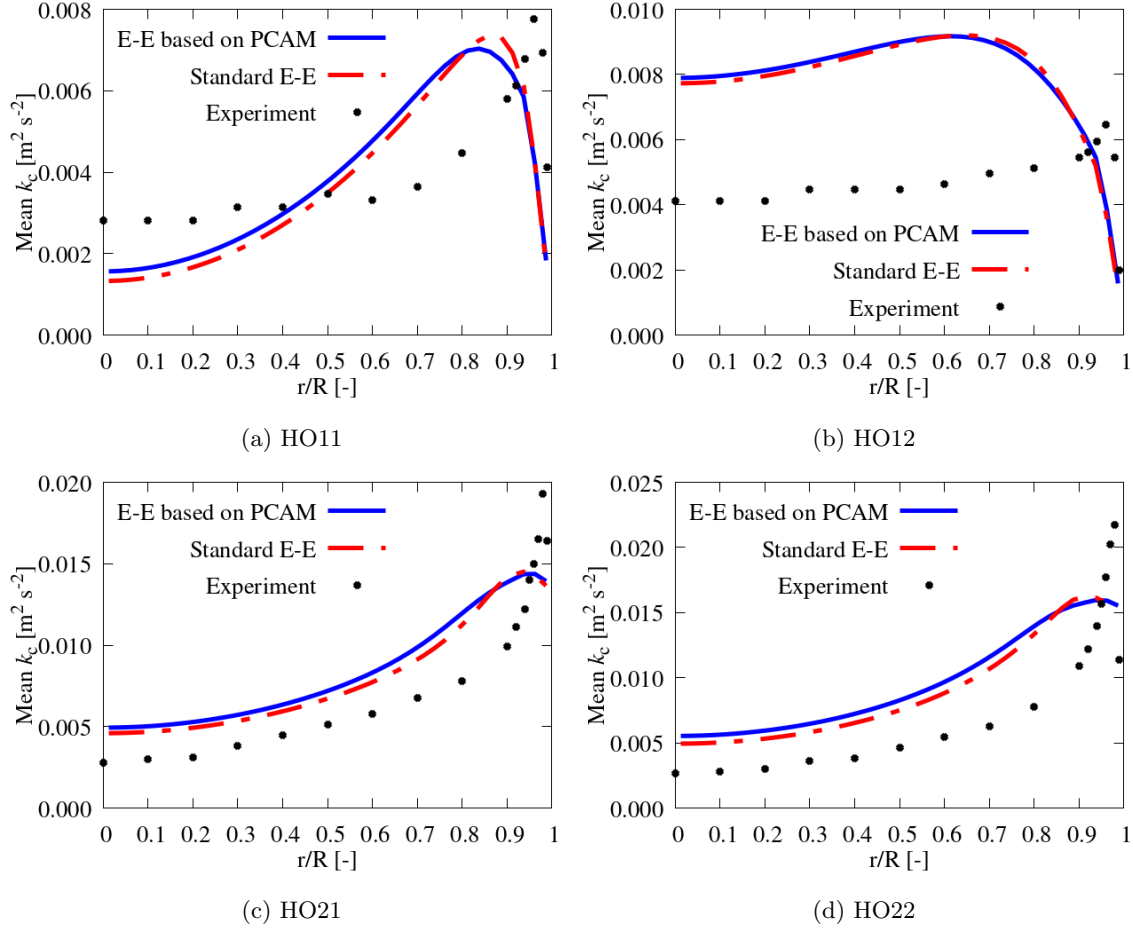


Fig. 8. Liquid Turbulence Kinetic Energy for Experimental Cases of Hosokawa et al. ("E-E": Euler-Euler model).

turbulence kinetic energies simulated with both Euler-Euler models are close to each other. For cases HO11 and HO12, the shape of the simulated profiles is different from the shape of the measurement ones. For cases HO21 and HO22, the shape of the simulated profiles is similar to that of the measurement ones except that the high wall peak in the measurement profiles is not reproduced in the simulation results.

IV. DISCUSSION AND CONCLUSION

A particle-center-averaged Euler-Euler model has been developed by combining a particle-center-averaged Euler-Euler framework with a Gaussian convolution method. With this combination, the particle-center-averaged Euler-Euler model can be employed for the two-phase flow

simulation with the bubble diameter larger than the computational cell spacing. To evaluate this approach, the results simulated with the particle-center-averaged Euler-Euler model and the standard Euler-Euler model are compared with experimental data for bubbly flows in two different vertical pipes. The results illustrate that when the bubble diameter is larger than the radial cell spacing, the radial gas volume fraction peak for the wall-peaking cases is over-predicted by the standard Euler-Euler model. Besides, the peak can be narrower than the peak in the experimental data. Using the particle-center-averaging method in Euler-Euler simulation alleviates the over-predictions of the gas volume fraction peaks and widens the peak for wall-peaking cases. These prove that using the particle-center-averaging method in the Euler-Euler model recovers the consistency of the bubble forces. The axial gas and liquid velocity as well as liquid turbulence kinetic energy simulated with both Euler-Euler models are close to each other.

In the validations, the particle-center-averaged Euler-Euler approach does not lead to better agreements for all bubbly flow cases because this approach solves only one problem for the bubbly flow modeling. The deviation between the simulation results and the experimental data may come from inconsistencies in the bubble force models and the measurement uncertainty in the experimental data. Further research to decrease the deviation is beyond the scope of this work.

ACKNOWLEDGMENTS

This work was supported by the China Scholarship Council (CSC) and partly supported by the Helmholtz European Partnering Program in the project "Crossing borders and scales (Crossing)".

REFERENCES

- [1] A. TOMIYAMA, H. TAMAI, I. ZUN, and S. HOSOKAWA, "Transverse migration of single bubbles in simple shear flows," *Chemical Engineering Science*, **57**, 1849 (2002).
- [2] S. HOSOKAWA, A. TOMIYAMA, S. MISAKI, and T. HAMADA, "Lateral migration of single bubbles due to the presence of wall," *ASME Fluids Engineering Division Summer Meeting*, Montreal, Canada (2002). July 14-18.

- [3] T. ZIEGENHEIN, A. TOMIYAMA, and D. LUCAS, “A new measuring concept to determine the lift force for distorted bubbles in low Morton number system: Results for air/water,” *International Journal of Multiphase Flow*, **108**, 11 (2018).
- [4] A. TOMIYAMA, N. SHIMADA, and H. ASANO, “Application of Number Density Transport Equation for the Recovery of Consistency in Multi-Field Model,” *4th ASME-JSME Joint Fluids Engineering Division Summer Meeting*, Honolulu, USA (2003). July 6-10.
- [5] R. LEHNIGK, “A generalized population balance model for the simulation of polydisperse multiphase flows within the Euler-Euler framework,” PhD Thesis, Technische Universität Dresden (2020).
- [6] D. ZHANG and A. PROSPERETTI, “Averaged equations for inviscid disperse two-phase flow,” *Journal of Fluid Mechanics*, **267**, 185 (1994).
- [7] A. PROSPERETTI, “Ensemble averaging techniques for disperse flows,” D. A. DREW, D. D. JOSEPH, and S. L. PASSMAN (Editors), *Particulate Flows*, 99–136, Springer. (1998).
- [8] A. TOMIYAMA, K. SAKODA, K. HAYASHI, A. SOU, N. SHIMADA, and S. HOSOKAWA, “Modeling and hybrid simulation of bubbly flow,” *Multiphase Science and Technology*, **18**, 73 (2006).
- [9] D. LUCAS, E. KREPPER, and H.-M. PRASSER, “Prediction of radial gas profiles in vertical pipe flow on the basis of bubble size distribution,” *International Journal of Thermal Sciences*, **40**, 217 (2001).
- [10] D. LUCAS, E. KREPPER, and H.-M. PRASSER, “Use of models for lift, wall and turbulent dispersion forces acting on bubbles for poly-disperse flows,” *Chemical Engineering Science*, **62**, 4146 (2007).
- [11] D. DARMANA, N. G. DEEN, and J. KUIPERS, “Parallelization of an Euler–Lagrange model using mixed domain decomposition and a mirror domain technique: Application to dispersed gas–liquid two-phase flow,” *Journal of Computational Physics*, **220**, 216 (2006).
- [12] Y. LAU, W. BAI, N. DEEN, and J. KUIPERS, “Numerical study of bubble break-up in bubbly flows using a deterministic Euler–Lagrange framework,” *Chemical Engineering Science*, **108**, 9 (2014).

- [13] R. SUN and H. XIAO, “Diffusion-based coarse graining in hybrid continuum–discrete solvers: Theoretical formulation and a priori tests,” *International Journal of Multiphase Flow*, **77**, 142 (2015).
- [14] R. SUN and H. XIAO, “Diffusion-based coarse graining in hybrid continuum–discrete solvers: Applications in CFD–DEM,” *International Journal of Multiphase Flow*, **72**, 233 (2015).
- [15] THE OPENFOAM FOUNDATION LTD., “OpenFOAM-dev,” <https://github.com/OpenFOAM/OpenFOAM-dev/tree/de9b29f0fdbb176cc31b8d466f60be3f4fb934de>, commit on 24. March (2021).
- [16] S. HÄNSCH, I. EVDOKIMOV, F. SCHLEGEL, and D. LUCAS, “A workflow for the sustainable development of closure models for bubbly flows,” *Chemical Engineering Science*, **244**, 116807 (2021).
- [17] A. D. BURNS, T. FRANK, I. HAMILL, and J.-M. SHI, “The Favre averaged drag model for turbulent dispersion in Eulerian multi-phase flows,” *5th International Conference on Multiphase Flow*, Yokohama, Japan (2004). May 30–June 4.
- [18] R. RZEHA, T. ZIEGENHEIN, S. KRIEBITZSCH, E. KREPPER, and D. LUCAS, “Unified modeling of bubbly flows in pipes, bubble columns, and airlift columns,” *Chemical Engineering Science*, **157**, 147 (2017).
- [19] M. ISHII and N. ZUBER, “Drag coefficient and relative velocity in bubbly, droplet or particulate flows,” *AIChE journal*, **25**, 843 (1979).
- [20] H. HESSENKEMPER, T. ZIEGENHEIN, R. RZEHA, D. LUCAS, and A. TOMIYAMA, “Lift force coefficient of ellipsoidal single bubbles in water,” *International Journal of Multiphase Flow*, **138**, 103587 (2021).
- [21] T. AUTON, J. HUNT, and M. PRUD’HOMME, “The force exerted on a body in inviscid unsteady non-uniform rotational flow,” *Journal of Fluid Mechanics*, **197**, 241 (1988).
- [22] F. R. MENTER, “Review of the shear-stress transport turbulence model experience from an industrial perspective,” *International Journal of Computational Fluid Dynamics*, **23**, 305 (2009).

- [23] T. MA, C. SANTARELLI, T. ZIEGENHEIN, D. LUCAS, and J. FRÖHLICH, “Direct numerical simulation-based Reynolds-averaged closure for bubble-induced turbulence,” *Physical Review Fluids*, **2**, 034301 (2017).
- [24] D. LUCAS, E. KREPPER, and H.-M. PRASSER, “Development of co-current air–water flow in a vertical pipe,” *International Journal of Multiphase Flow*, **31**, 1304 (2005).
- [25] H. PRASSER, D. LUCAS, E. KREPPER, D. BALDAUF, A. BÖTTGER, U. ROHDE, P. SCHÜTZ, F. ZIPPE, W. ZIPPE, and J. ZSCHAU, “Flow maps and models for transient two-phase flows,” , Forschungszentrum Rossendorf e.V. (2003).
- [26] S. HOSOKAWA and A. TOMIYAMA, “Multi-fluid simulation of turbulent bubbly pipe flows,” *Chemical Engineering Science*, **64**, 5308 (2009).
- [27] T. ZIEGENHEIN and D. LUCAS, “The critical bubble diameter of the lift force in technical and environmental, buoyancy-driven bubbly flows,” *International Journal of Multiphase Flow*, **116**, 26 (2019).
- [28] R. RZEHAKE, Y. LIAO, R. MELLER, F. SCHLEGEL, R. LEHNIGK, and D. LUCAS, “Radial pressure forces in Euler-Euler simulations of turbulent bubbly pipe flows,” *Nuclear Engineering and Design*, **374**, 111079 (2021).
- [29] Y. LIAO, K. UPADHYAY, and F. SCHLEGEL, “Eulerian-Eulerian two-fluid model for laminar bubbly pipe flows: Validation of the baseline model,” *Computers & Fluids*, **202**, 104496 (2020).